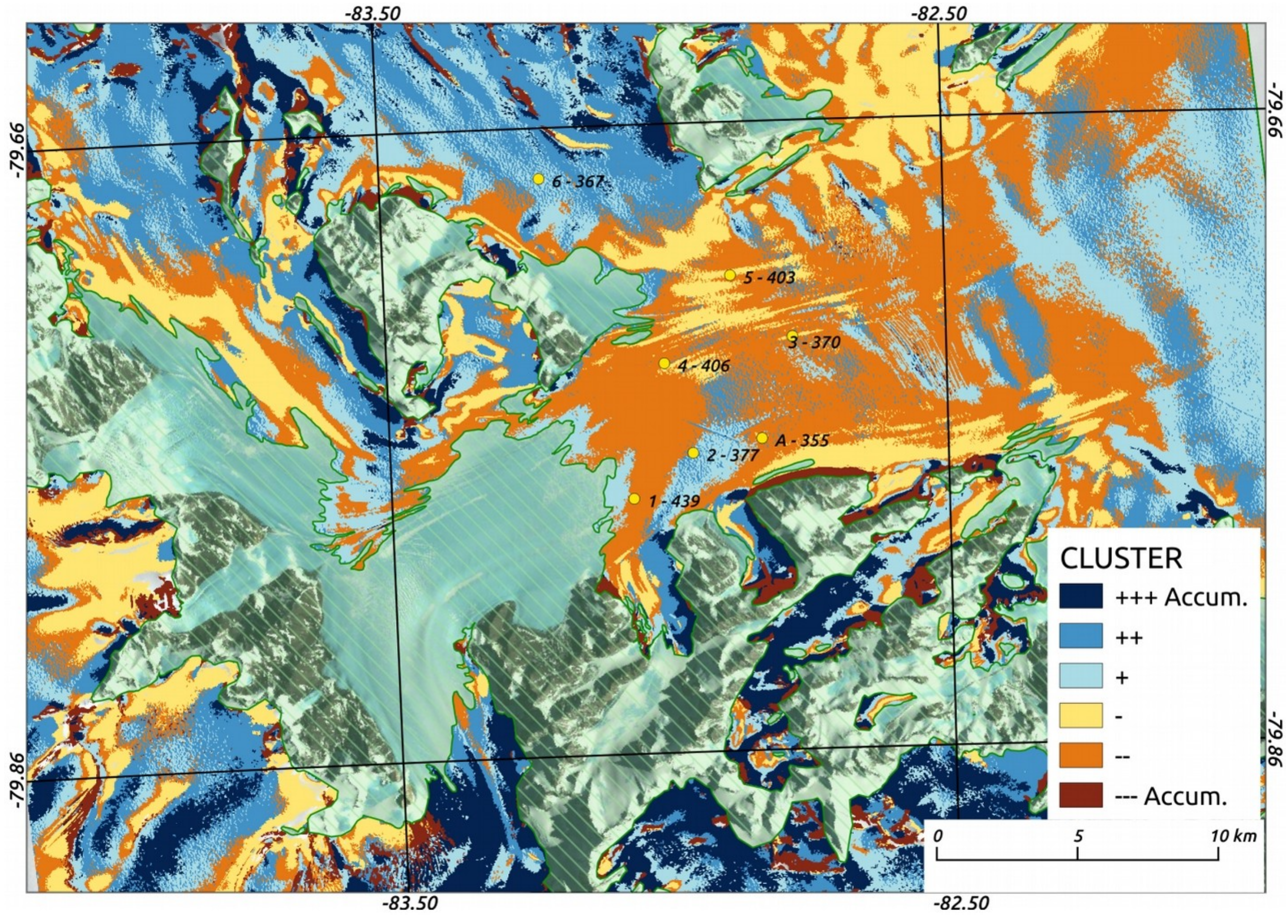

Figure 14: Cluster classification that was conducted with the averaged sigma SAR image and terrain products as input and six classes. The colour code is the relative accumulation rate between areas and is set as the previous classification. Compared to the previous classification, a broader and homogeneous zone of lower accumulation (orange) existed in the central valley downward from the BIA, including SP1 and SP4. The red class is restricted to specific areas close to the mountain.

The same flux features appeared in the zone between SP3 and SP5. We observed these features in the final classification because the TanDEM-X DEM was used. We evaluated the surface profile, and not all changes in the classes were responses to changes in the slope/aspect at the surface. We also tested terrain flattening in the image pre-processing chain by using the SNAP software with both TanDEM-X and REMA, but the additional processing did not remove these features from the SAR image.

4. Discussion

4.1. AWS and Snow Depth

The AWS record (2014-2017) showed no marked accumulation season, although we noticed a significant episode of accumulation that began in autumn and lasted until late spring. Except for 2014, most of the accumulation was deposited in very few events, similar to what was observed by Reijmer & Broeke (2003) in Droning Maud Land closer to the coast at lower elevation. The SMB was within the range of previous estimates. Despite the short observation period, temporal variability existed, with 50% less accumulation in 2017 compared to 2014.

Previous meteorological records have been available from AWS Wx7 since 2010, which was replaced by Wx14 in 2014 and is operated by the private company Antarctic Logistics and Expeditions (ALE) at the Union Glacier ice runway (79°45.93' S, 83°13.58' W, 705 m asl). Unfortunately, no snow accumulation was recorded. Importantly, both the Wx7/14 and UNION13 stations are located in the central valley, but the stations are 15 km apart. The former is located in the runway in the BIA area on the northern side of the central valley and upstream, where the wind is stronger. Rivera et al. (2014) used these station data to describe the meteorological conditions in their work. The latter station is located close to operational support at the Chilean base camp. Hence, we assumed a predominant wind direction of 255º for the wind-effect index based on our records instead of 225º, as reported by Rivera et al. (2014).

The meteorological data, despite the short collection period, provided climate trends and unique in-situ data on the regional climate conditions. UNION13's location is suitable for building a unique long-term record of snow accumulation with high temporal resolution. In contrast to the runway's location, an area with zero or negative mass balance, UNION13 is located in the central valley downward from the basin catchment and downward from the BIA, where the SMB increases.

4.2. Snowpit

Three types of grains were present: irregular, rounded and faceted. We did not observe precipitated grain types that were preserved in any stratigraphic profile, even Graupel. Graupel grains are the most stable form because of their low surface/volume ratio, which allows them to be preserved for extended periods in the snowpack with less metamorphism. This finding indicates the dominant role of wind on depositional processes because of transport or metamorphism agents. Irregular crystals are a varying crystal type that are no longer recognized and are already within a grade of metamorphism in the snowpack. Rounded crystals indicate a later stage of metamorphism, where the grain grows at the expense of smaller particles. However, this finding also indicates drifted snow. Faceted crystals indicate constructive metamorphism, which is driven by temperature gradients and water vapour. Faceted crystals also indicate a layer that is exposed to wind for a longer period at the surface, especially during winter, when the air humidity is low; the intense wind blowing at the surface acts to remove water vapour, generating a vapour gradient that consequently favours constructive metamorphism. Thus, we can interpret faceted crystals as wind-exposed depositional areas.

This assumption agrees with the field knowledge, where we observed sites that were less exposed to wind in SP2 and SP6 (Figure S2 and Figure S6), and we rarely observed faceted crystals. The average small grain sizes ranged between 0.5 and 1.0 mm, and both profiles exhibited fewer layers, which were usually more extensive than in other SPs, indicating a higher load of deposition per event. Interestingly, we also noted a difference between the two sites. Rounded forms were dominant in SP6, which is located inside the tributary Driscoll Glacier, whereas irregular snow crystal types were more frequent in SP2 on the opposite side of the main trunk of UG. The potential reason was the supplied mass source into these two environments. In Driscoll, the snow is drifted/transported a longer distance and eroded to rounded forms. In addition to a more protected area because of the U-shaped valley with an orientation transverse to the predominant wind direction, we note smaller particle sizes as an effect of the position at the leeward side of the mountain, as observed by Ingvander et al. (2016), decreasing the wind-transport potential. The grain-size range that was observed in our field data matched that in Ingvander et al. (2016) along the coastal zone in Droning Maud Land. These authors found larger grain sizes compared to those in the higher plateau section, where higher accumulation was observed. Additionally, the transitional-zone samples and the first ascending polar-plateau samples were smaller and more homogeneous, which could have caused by the position of the samples in the mountain range or on the leeward side of the mountain range facing the plateau. In the same manner, our samples in areas that were less exposed to wind, e.g., SP2 and SP6, exhibited smaller and more homogeneous grain sizes.

Distinct layers of snow built up in the snowpack because of the intermittent nature of precipitation, the action of wind and continuously ongoing metamorphism of snow. Each stratigraphic layer differed from the adjacent layers above and below in terms of the microstructure and/or density, which together define the snow type, snow hardness, and snow temperature (Fierz *et al.* 2009). Therefore, we can interpret each layer as a distinct depositional event at any one time because the physical and mechanical properties depend on these characteristics. Palais et al. (1982) studied snow stratigraphy at Dome C and recognized a thin crust as a proxy to identify annual layers because this type of thin crust is usually produced at the surface in late summer and subsequently buried, although such crusts may no longer be easily recognizable after firnification. We did not find evidence of the cyclic layer to be well marked with a thin hard crust. At SP3 (Figure S3), two hard crusts covered a soft crust (i.e., fist hardness) in the first 40 cm, each layer being 20 cm thick. However, based on the amount, this finding probably represents two distinct, short events and not the majority of the annual accumulation. As shown in the UNION13 AWS records, the snow accumulation varied throughout the year, with sporadic depositional events and continued sublimation/erosion (Figure 4). The larger number of layers in the 2-m depth interval indicates several deposition events in the years with low amounts, where each layer was exposed to the air-snow interface for a longer time and metamorphism more intensely differentiated the layers. Thus, the annual SMB could not be estimated for every snowpit.

Density profiles can reveal transitions between layers through high-amplitude inflections. Harper & Bradford (2003) Compared the number of layers that were identified by both methods under the same sampling resolution and observed twice as many layers in a density profile through a permittivity probe. The errors that were associated with sampling and weighing the volume of snow were approximately 10% (Harper & Bradford 2003). In our data, we observed many more stratigraphic layers than density inflections, considering the low sampling resolution of 10 cm. Because of the air temperature's seasonal cycle, the gradient between the snow surface and atmosphere increased by the end of summer and the beginning of autumn, and densification intensified. Therefore, a high inflection of high-density layers could be approximately traced as a single year's SMB, but we could not confirm this point. However, we have four to five years of accumulation in the first 2 m of SP2, in contrast to the five to six years of accumulation based on the age model that was used by Hoffmann et al. ('in review') close to the EPCCGU. This difference can be within the accuracy in the age model because of inter-annual accumulation variability. McMorrow et al. (2002) highlighted the inter-annual accumulation variability at Law Dome (East Antarctica) and outlined its implications for interpreting the ice-core record. The short period in the 2-m snowpits does not represent the inter-annual variability, and the influence of the inter-annual variability on the spatial variability cannot be isolated.

4.3. SAR

The differences that were observed in the backscattering indicated differences in snowpack morphology. Rott et al. (1993) found low backscattering coefficients for areas with permanent dry snow, high accumulation rates, and homogeneous snow morphology. Our interpretations of SP2 and SP6 matched, and these areas displayed low backscattering in the SAR images. West of the Chilean base camp EPCCGU was a brighter patch that appeared as a wind track (red arrow in Figure 7), which originates from the small tributary to the southwest of the "Criosfera Glacier". Consequently, the higher backscattering suggests a zone of higher density and grain size. The interpretation of a wind track makes sense, whereas a darker patch of a wind-protected zone was present on the eastern side, which was elected by ALE and Chile as a base-camp site.

We investigated the enhanced glacial-flow structure in the SAR images. Some of the contrasting areas that changed from low to high backscattering were followed by changes in the surface elevation in the TanDEM-X. We initially believed that the explanation could be the alignment of the surface aspect at a right angle to the SAR antenna (the satellite azimuth was from right to left and nearly parallel to the valley flow). The surface aspect reduced the incident angle, increasing the surface-scatter contribution. For frequencies below 10 GHz, scattering losses are neglected, and volume scatters are dominant (Rott et al. 1993). The main argument resulted from the low contrast between layers (Du *et al.* 2010). Forster et al. (1999) quantified a volume scatters contribution of 100% (>95% for 25º) with an incident angle greater than 30º. We checked the incident angle in the geometrically corrected SAR image, and the angle varied only in the range of 22-26º between areas of low and high backscattering. As we presented in the results based on the SAR simulated image, the surface relief was smoother than what was represented by TanDEM-X. Therefore, TanDEM-X were representing some changes in the subsurface. We examined a GPR transect that crossed these zones and found that the backscattering varied with the snow-ice horizon depth (data not published yet). The backscattering increased where the snowpack was thinner than 10 m deep because some of the signal is reflected by the ice back to the snowpack, increasing the volume scatter. The terrain-flattening process, which normalizes the returning signal by using locally illuminated areas, did not smooth these features in the SAR images.

Another fact that could have enhanced the flow features would be converging fluxes from tributaries enhancing the contrast vertically and horizontally between deeper layers, increasing the multilayer scattering. According to Tsang et al. (2006), multiple scattering can raise signals by a few decibels if the scattering albedo is close to one. Dierking et al. (2012) found few test sites with albedo values larger than 0.7 in the C-band and 0.8 in the Ku-band. In these cases, the accumulation rates were low, and high scattering albedo was located at greater depths (caused by larger grains). At specific locations in Greenland and Antarctica, deep hoars formed at the onset of summer (comparatively larger grain sizes, 2-5 mm). In addition, the northern side of the valley had a shallower firn layer, and we expect a higher density gradient in the first ten meters within the SAR signal.

Comparing the snow density and grain-size maps with the field data did not indicate absolute correspondence. The applied algorithm overestimated the density over the snowpit density (Figure 10). The field measurements corresponded to the first 2 m and were averaged from the 10-cm measurements without considering the thickness of each layer. The attenuation depth of the X-band can reach 10 m in areas of dry snow (Rott *et al.* 1993, Wessel *et al.* 2016), so the signal probably interacts with denser layers beyond the first 2 m, although Espinoza et al. (2014) estimated that most backscattering (<95%) occurs in the initial 2 m of a package. A density profile that was derived from a firn core (indicated by a green dot in

Figure 10) close to SP2 showed densities from 400 kg m^{-3} at the surface to 550 kg m^{-3} at a depth of 8 m (Hoffmann et al. 'in review'), which was more similar to the algorithm-derived density than the average field density. The density map alone did not appear to explain the variations in the snowpack; for example, SP3 and SP5 are interpreted as being in high-density (SAR-derived) areas because of high backscattering, but other characteristics, such as the grain size and number of layers, likely contribute to the high backscattering in addition to the density. For example, SP3 and SP5 had larger grains and more layers than SP2 and SP6, indicating lower accumulation rates than those in SP2 and SP6. A lower accumulation rate will tend to develop larger grain sizes for snow because each snow layer is exposed at the surface for a longer period (Linow *et al.* 2012).

In addition, the map indicated that SP2 and SP6 had the same density values of approximately 440 kg m-^{3}, but the field densities were 417 kg m^{-3} and 338 kg m^{-3}, respectively. Similarly, SP1 and SP4 also had density values in the same range of 520-570 kg m^{-3}, but the field density differed from 433 kg m^{-3} to 400 kg m^{-3}, respectively. Despite this disagreement between the two datasets, the mean density of the 2-m snowpits matched the stratigraphic interpretation if we considered the southern side of the valley (SP1, SP2 and SPA) separately from the northern side (SP3, SP4, SP5, and SP6). On the southern side, SP1 and SP2 differed in terms of density, corresponding to a higher density at SP1 because of wind compaction and a lower density at SP2. On the northern side, the density range differed from that on the southern side, but a gradient existed, with higher values in SP4 decreasing to those in SP3, SP5 and SP6. These differences were likely influenced by other characteristics, such as the grain type and wind transport between the southern and northern sides.

SPA had a low mean density, and many layers could explain the higher backscattering. We hypothesized that SPA is located at a wind-protected site (white circle in Figure 10) leeward from Rossmann Mountain, where the amount of snow that accumulates originates from blowing snow that bypasses the topographic barrier, which reflects the small grain size that was observed in the stratigraphic analysis. Because the amount of snow in each depositional event was small, the snow was metamorphosed in the first centimetres because of the longer exposure time, creating a layered snowpack. On the northern side of the central valley, SP4 exhibited approximately the same backscattering value as SP1 but a lower density, which was caused by hypothetical wind compaction that was lower than that on the other side of the valley. Compared to SP4, SP1 showed more hard layers in the first meters. SP4 also showed hard layers, which were intercalated with softer layers. The lower density at SP3 downwind from SP4 could indicate the drifting of snow from SP4 to SP3, increasing accumulation at SP3. The greater number of layers compared to SP4 and the large grain size could explain the high level of backscattering at this site.

4.4. Terrain products

The aspect map clearly contrasted the right side of the wind track with intercalating bright values (1), indicating pixels with windward orientations (Figure 12c), which extended to SP2. However, the darker colours (-1) along the wind track indicated a leeward aspect. This difference explained the change in accumulation between SP1 and SP2: leeward snow tended to be carried away, whereas windward surfaces tended to accumulate snow. Goodwin (1990) showed that accumulation rates are higher on windward slopes than leeward slopes. In fact, SP2 and SP6 were located in areas with a windward aspect, while SP1 had a leeward aspect. However, SP4 contrasted what was expected in terms of the windward aspect, and SP5 had a leeward aspect. These slope values explain why SP4 (SP5) had lower (higher) accumulation even in a windward (leeward) area. The slope values for both locations were lower than those for the other sites (Figure 12d).

Accumulated snow is deposited in the form of surface microrelief as topographic features on spatial scales of 10-100 m (Goodwin 1990). These features reflect higher slope values, corresponding to areas where we expect higher accumulation. We observed a low-slope area that extended from SP1 in the wind-track zone, crossing the valley to the surrounding area of SP4 (Figure 12d.). We interpreted this zone as a flat surface because of wind action with lower accumulation. The roughness was similar to the slope. Higher surface roughness favours snow deposition in intercalating high- and low-pressure surfaces, promoting turbulent air fluxes (Frezzotti *et al.* 2002).

The wind-effect algorithm considers a fixed mean wind direction for the entire grid and might not perfectly represent local conditions that are related to katabatic winds, which tend to follow the topography. The algorithm also depends on the search distance; varying this distance enables us to obtain more or less wind shelter in the tributary of the Schanz and Driscoll glaciers. In the Driscoll valley, as observed at SP6, the snow deposition was dominated by small grains that bypassed hills and were further deposited. Using a high search distance in the wind-effect algorithm ignores the adaptability of wind streams to the land surface (Böhner and Antonić 2009). The 255º wind-effect map corresponded better to the main trunk valley direction and therefore represents the effect of katabatic wind moving down the glacier (Figure 12b). This map adequately represents intercalated zones that are more and less exposed to wind down the valley. The wind-effect field was also more exposed at SP4. SP5 and SP3 were located directly adjacent to an area that was exposed to wind. These locations mean that these areas received blown snow from wind-exposed areas. Figure 12b does not show a higher wind exposure at SP1 or a lower exposure at SP2, as we would expect. However, we interpreted the algorithm results as generally exposed to the wind, which means that the algorithm tended to interpret the surface that was sloped windward as exposed and the surface that was sloped leeward as sheltered. This determination makes sense, for example, at the border outside the masked area with low backscattering values in the SAR image (Figure 7). This area is located directly beyond a wind-exposed area in the BIA and receive blowing snow, similar to SP5 and SP3. On a local scale, the algorithm could not consider the effect of the slope and topography when modelling wind-direction changes because the algorithm considers only a fixed wind direction. Most likely, local features such as the wind that flow down through the smaller valleys and throats were not modelled. For example, we note the slight difference between the mean wind directions that were reported by Rivera et al. (2014) at the runway and in our work at the UNION13 AWS.

4.5. Cluster

We masked 32% of the 1687-km² imaging area as mountainous/sloped area and BIA, both of which showed low and negative accumulations, respectively. Approximately 41% of the area was classified as high accumulation and 28% was classified as low accumulation (Table IV). Most of the ablation stakes that were used to infer the mass balance of Union Glacier in previous studies (Rivera et al. 2014) were located in areas that were considered to be low accumulation, which would suggest that the mass balance could be higher than previously thought if we considered zones with high accumulation rates. Field observations indicated that this difference could reach 0.1 m w.e. a^{-1}, affecting the net mass balance for the area by as much as 0.041 m w.e. a^{-1}. Further work will investigate a 72-km-long profile along the glacier, which will provide quantification and comparisons between the different depositional zones. The results help to identified different area and can guide future works on the attenuation depth in dry snow to better correct new DEMs that are derived from TanDEM-X interferometry (Wessel *et al.* 2016).

Table IV: Area of each cluster class and percentage of the total imaging area.

	km^2	%
Masked	536.4	31.8
+++ Accum.	175	10.4
++	254.5	15.1
+	255.6	15.1
-	151.2	9
--	255.9	15.2
--- Accum.	59	3.5
TOTAL	1687.4	100

If we consider this dynamic for the entire Ellsworth Mountain Range, which comprises four significant basins from MEaSURE Antarctica Boundaries, including the Rutford, Minnesota, Union, and Hercules glaciers, we have a total area of 85,800 km^2. Considering the central glacial valleys exclusively as the study area, we found that ~12,000 km^2 (6,000 Sentinel Range and ~6,000 Heritage Range) of the total 85,800-km^2 area should have the same high spatial variability of snow accumulation. Thus, we would have a masked area of roughly 2,048 km^2 from the ADD rocky area (or only a 378-km^2 base on the Landsat 8 rocky area), 35 km^2 from the ADD moraine area and 612 km^2 of BIA, which corresponds to 22%. An example of the importance of considering the variability of SMB was demonstrated by (Frezzotti *et al.* 2004) in East Antarctica. High spatial variability was observed because of wind-driven sublimation; consequently, previous SMB maps that did not consider these factors overestimated the SMB.

5. Conclusions

Our results showed that wind-exposed areas had larger snow grains (i.e., 1-4 mm versus 0.5-1 mm in wind-protected areas), faceted forms from greater exposure to the temperature gradient, more deposition layers and layers with greater hardness. The densification processes in these areas were more intense and produced thicker hard layers.

The stratigraphic profiles and the density and grain-size maps confirmed a distinct pattern of snowpack characteristics, which further indicated particular depositional rates along the glacier. The field interpretations guided us to delimit different depositional zones, and an initial cluster analysis successfully classified SAR backscattering into six classes. Some zones were classified as low accumulation-rate zones because of high backscattering, although the field data suggested a higher accumulation rate. We introduced terrain products to better isolate these zones in the cluster classification, which were directly related to or influenced the depositional process. Roughness data were a good indicator of the deposition dynamics. The wind effect was limited to representing local wind flow and provided only a general scenario but failed to explain the local variations in the depositional zone. In addition to wind exposure, we had to consider where the wind was blowing. If the wind was channelled through throats without lifting snow for later deposition, the wind would erode and flatten the surface into a wind-glazed surface, as observed in the wind-track area close to SP1.

The SAR image significantly enhanced the glacier-flow features, especially in the zone of converging fluxes. A simulated SAR image was generated with the TanDEM-X DEM and the REMA DEM. The later did not produce such features, indicating that the cause of the high backscattering may have been in the subsurface. The features probably reduced the volume-scatter contribution, increasing surface reflectance in the multi-layered media; thus, the SAR signals in such zones must be carefully interpreted.

The imaged area focused on the mountainous area of the glacial basin, and up to 40% of the areas were masked. This high percentage indicates that a significant area might not represent the mean SMB from the coarse-resolution data. Moreover, these masked areas corresponded to 172 km² of BIAs (10%), where we expected to find a negative mass balance. The other component was mountainous/rocky areas with a steep slope and likely lower rates of accumulation. These areas represented 469 km^2 (16%) of the total basin area of 2955 km^2, or 690 km^2 if we considered the MEaSURE Antarctica Boundaries.

These results should assist future investigations of SMB variability and could influence or act as a significant factor in interpolating this variable in climate models. These results can also guide future works on the attenuation depth in dry snow to better correct new DEMs that are derived from TanDEM-X interferometry. Future work will investigate the accumulation rate by using GPR. The accumulation rate could be calibrated by comparing AWS snow-depth data with annual snowpit and GPR profiles. A total of 72 km of GPR profiles will facilitate the quantification of the accumulation variations along the glacier.

Funding and Acknowledgements

This work was supported by the National Council for Scientific and Technological Development (CNPq) [projects 461414/2014-7 and 441810/2016-0], INCT da Criosfera and the Research Support Foundation of the Rio Grande do Sul State (FAPERGS) [17/2551-0000518-0]. Instituto Antártico Chileno and Fuerza Aérea Chilena are acknowledged for logistical support during the summer campaigns at Union Glacier. The Italian Space Agency and German Aerospace Centre allowed access to the CSK imagery and the TanDEM-X digital elevation models, respectively.

Description of the authors' responsibilities

JAN and RJ collected the field data. CFG processed the data and wrote the major components of the paper. CFG and JAN jointly led the study. All the authors contributed to and revised the manuscript at all stages.

References

Arthern, R.J., Winebrenner, D.P. & Vaughan, D.G. 2006. Antarctic snow accumulation mapped using polarization of 4.3-cm wavelength microwave emission. *Journal of Geophysical Research: Atmospheres*, **111**, 1–10, 10.1029/2004JD005667.

Böhner, J. & Antonić, O. 2009. Chapter 8 Land-Surface Parameters Specific to Topo-Climatology. *In Developments in Soil Science*. 195–226., 10.1016/S0166-2481(08)00008-1.

Burton-Johnson, A., Black, M., Peter, T.F. & Kaluza-Gilbert, J. 2016. An automated methodology for differentiating rock from snow, clouds and sea in Antarctica from Landsat 8 imagery: A new rock outcrop map and area estimation for the entire Antarctic continent. *Cryosphere*, **10**, 1665–1677, 10.5194/tc-10-1665-2016.

Dadic, R., Mott, R., Lehning, M. & Burlando, P. 2010. Wind influence on snow depth distribution and accumulation over glaciers. *Journal of Geophysical Research: Earth Surface*, **115**, 1–8, 10.1029/2009JF001261.

Dierking, W., Linow, S. & Rack, W. 2012. Toward a robust retrieval of snow accumulation over the Antarctic ice sheet using satellite radar. *Journal of Geophysical Research: Atmospheres*, **117**, 1–17, 10.1029/2011JD017227.

Ding, M.H., Xiao, C. De, Li, C.J., Qin, D.H., Jin, B., Shi, G.T., Xie, A.H. & Cui, X. Bin. 2015. Surface mass balance and its climate significance from the coast to Dome A, East Antarctica. *Science China Earth Sciences*, **58**, 1787–1797, 10.1007/s11430-015-5083-9.

Ding, M.H., Zhang, T., Xiao, C. De, Li, C.J., Jin, B., Bian, L.G., Wang, S.J., Zhang, D.Q. & Qin, D.H. 2017. Snowdrift effect on snow deposition: Insights from a comparison of a snow pit profile and meteorological observations in east Antarctica. *Science China Earth Sciences*, **60**, 672–685, 10.1007/s11430-016-0008-4.

Du, J., Shi, J. & Rott, H. 2010. Comparison between a multi-scattering and multi-layer snow scattering model and its parameterized snow backscattering model. *Remote Sensing of Environment*, **114**, 1089–1098, 10.1016/j.rse.2009.12.020.

Espinoza, J., Arigony-Neto, J. & Jana, R. 2014. SAR backscatter model inversion for estimation of snow properties along the Union Glacier — Antarctica. *IEEE Geoscience and Remote Sensing Symposium*, 3980–3982, 10.1109/IGARSS.2014.6947357.

Fassnacht, S.R., López-Moreno, J.I., Toro, M. & Hultstrand, D.M. 2013. Mapping snow cover and snow depth across the Lake Limnopolar watershed on Byers Peninsula, Livingston Island, Maritime Antarctica. *Antarctic Science*, **25**, 157–166, 10.1017/S0954102012001216.

Fierz, C., Armstrong, R.L.L., Durand, Y., Etchevers, P., Greene, E., McClung, D.M.M., Nishimura, K., Satyawali, P.K.K. & Sokratov, S. A. A. 2009. The International Classification for Seasonal Snow on the Ground. *IHP-VII Technical Documents in Hydrology*, **83**, 90, http://www.cosis.net/abstracts/EGU05/09775/EGU05-J-09775.pdf.

Forster, R.R., Jezek, K.C., Bolzan, J. & Baumgartner, F. 1999. Relationships between radar backscatter and accumulation rates on the Greenland ice sheet. *Int. J. Remote Sens.*, **20**, 3131–3147.

Frezzotti, M., Gandolfi, S. & Urbini, S. 2002. Snow megadunes in Antarctica: Sedimentary structure and genesis. *Journal of Geophysical Research: Atmospheres*, **107**, 1–12, 10.1029/2001JD000673.

Frezzotti, M., Pourchet, M., Flora, O., Gandolfi, S., Gay, M., Urbini, S., Vincent, C., et al. 2004. New estimations of precipitation and surface sublimation in East Antarctica from snow accumulation measurements. *Climate Dynamics*, **23**, 803–813, 10.1007/s00382-004-0462-5.

Frezzotti, M., Urbini, S., Proposito, M., Scarchilli, C. & Gandolfi, S. 2007. Spatial and temporal variability of surface mass balance near Talos Dome, East Antarctica. *Journal of Geophysical Research: Earth Surface*, **112**, F02032, 10.1029/2006JF000638.

Fujiwara, K. & Endo, Y. 1971. Preliminary report of glaciological studies. *Report of the Japanese traverse, Syowa South Pole 1968-1969*, 68–109.

Fyke, J., Lenaerts, J.T.M. & Wang, H. 2017. Basin-scale heterogeneity in Antarctic precipitation and its impact on surface mass variability. *The Cryosphere*, **11**, 2595–2609, 10.5194/tc-11-2595-2017.

Goodwin, I.D. 1990. Snow accumulation and surface topography in the katabatic zone of Eastern Wilkes Land, Antarctica. *Antarctic Science*, **2**, 235–242, 10.1017/S0954102090000323.

Groot Zwaaftink, C.D., Cagnati, A., Crepaz, A., Fierz, C., MacElloni, G., Valt, M. & Lehning, M. 2013. Event-driven deposition of snow on the Antarctic Plateau: Analyzing field measurements with SNOWPACK. *Cryosphere*, **7**, 333–347, 10.5194/tc-7-333-2013.

Harper, J.T. & Bradford, J.H. 2003. Snow stratigraphy over a uniform depositional surface: Spatial variability and measurement tools. *Cold Regions Science and Technology*, **37**, 289–298, 10.1016/S0165-232X(03)00071-5.

Hofer, R. & Mätzler, C. 1980. Investigations on snow parameters by radiometry in the 3- to 60-mm wavelength region. *Journal of Geophysical Research: Oceans*, **85**, 453, 10.1029/JC085iC01p00453.

Hoffmann, K., Fernandoy, F., Meyer, H., Thomas, E.R., Aliaga, M., Tetzner, D., Freitag, J., et al. Stable water isotopes and accumulation rates in the Union Glacier region, West Antarctica over the last 35 years. *The Cryosphere Discussions*, 1–32, 10.5194/tc-2018-161.

Hui, F., Ci, T., Cheng, X., Scambos, T.A., Liu, Y., Zhang, Y., Chi, Z., et al. 2014. Mapping blue-ice areas in Antarctica using ETM+ and MODIS data. *Annals of Glaciology*, **55**, 129–137, 10.3189/2014AoG66A069.

Ingvander, S., Jansson, P., Brown, I.A., Fujita, S., Sugyama, S., Surdyk, S., Enomoto, H., Hansson, M. & Holmlund, P. 2016. Snow particle sizes and their distributions in Dronning Maud Land, Antarctica, at sample, local and regional scales. *Antarctic Science*, **28**, 219–231, 10.1017/S0954102015000589.

Linow, S., Hörhold, M.W. & Freitag, J. 2012. Grain-size evolution of polar firn: A new empirical grain growth parameterization based on X-ray microcomputer tomography measurements. *Journal of Glaciology*, **58**, 1245–1252, 10.3189/2012JoG11J256.

McMorrow, A.J., Curran, M.A.J., Van Ommen, T.D., Morgan, V.I. & Allison, I. 2002. Features of meteorological events preserved in a high-resolution Law Dome (East Antarctica) snow pit. *Annals of Glaciology*, **35**, 463–470, 10.3189/172756402781816780.

Palais, J.M., Whillans, I.M. & Bull, C. 1982. Snow Stratigraphic Studies At Dome C, East Antarctica: An Investigation Of Depositional and Diagenetic Processes. *Annals of Glaciology*, **3**, 239–242, 10.3189/S0260305500002846.

Pettinato, S., Santi, E., Brogioni, M., Paloscia, S., Palchetti, E. & Chuan Xiong. 2013. The Potential of COSMO-SkyMed SAR Images in Monitoring Snow Cover Characteristics. *IEEE Geoscience and Remote Sensing Letters*, **10**, 9–13, 10.1109/LGRS.2012.2189752.

Plattner, C.H., Braun, L.N. & Brenning, A. 2004. Spatial variability of snow accumulation on Vernagtferner, Austrian Alps, in winter 2003/2004. *Zeitschrift fuer Gletscherkunde und Glazialgeologie*, **39**, 43–57 Available at: http://www.geophysik.uni-muenchen.de/Members/plattner/publicationdetails/581%5Cnhttp://www.environment.uwaterloo.ca/u/brenning/Plattner-et-al-2006-ZGletscherk.pdf.

Rees, W.G. 2005. *Remote sensing of snow and ice*. CRC press.

Rivera, A., Zamora, R., Rada, C., Walton, J. & Proctor, S. 2010. Glaciological investigations on Union Glacier, Ellsworth Mountains, West Antarctica. *Annals of Glaciology*, **51**, 91–96, 10.3189/172756410791392772.

Rivera, A., Zamora, R., Uribe, J. a., Jaña, R. & Oberreuter, J. 2014. Recent ice dynamic and surface mass balance of Union Glacier in the West Antarctic Ice Sheet. *The Cryosphere*, **8**, 1445–1456, 10.5194/tc-8-1445-2014.

Rott, H., Sturm, K. & Miller, H. 1993. Active and passive microwave signatures of Antartic firn by means of field measurements and satellite data. *Annals of Glaciology*, **17**, 337–343 Available at: http://www.igsoc.org:8080/annals/17/igs_annals_vol17_year1993_pg337-343.pdf.

Shi, J. & Dozier, J. 2000. Estimation of snow water equivalence using SIR-C/X-SAR. II. Inferring snow depth and particle size Hayasaka, T., Wu, D.L., Jin, Y. & Jiang, J., *eds. IEEE Transactions on Geoscience and Remote Sensing*, **38**, 2475–2488, 10.1109/36.885196.

Tsang, L., Pan, J., Liang, D., Li, Z. & Cline, D. 2006. Modeling Active Microwave Remote Sensing of Snow using Dense Media Radiative Transfer (DMRT) Theory with Multiple Scattering Effects. *In 2006 IEEE International Symposium on Geoscience and Remote Sensing*. IEEE, 477–480., 10.1109/IGARSS.2006.127.

van de Berg, W., van den Broeke, M., Reijmer, C.H. & van Meijgaard, E. 2006. Reassessment of the Antarctic surface mass balance using calibrated output of a regional atmospheric climate model. *Journal of Geophysical Research: Atmospheres*, **111**, 1–15, 10.1029/2005JD006495.

Wendt, A., Casassa, G., Rivera, A. & Wendt, J. 2009. Reassessment of ice mass balance at Horseshoe Valley, Antarctica. *Antarctic Science*, **21**, 505, 10.1017/S0954102009002053.

Wessel, B., Bertram, A., Gruber, A., Bemm, S. & Dech, S. 2016. a New High-Resolution Elevation Model of Greenland Derived From Tandem-X. *ISPRS Annals of Photogrammetry, Remote Sensing and Spatial Information Sciences*, **III-7**, 9–16, 10.5194/isprsannals-III-7-9-2016.

Wessel, B., Huber, M., Wohlfart, C., Marschalk, U., Kosmann, D. & Roth, A. 2018. Accuracy assessment of the global TanDEM-X Digital Elevation Model with GPS data. *ISPRS Journal of Photogrammetry and Remote Sensing*, **139**, 171–182, 10.1016/j.isprsjprs.2018.02.017.

Winstral, A., Elder, K. & Davis, R.E. 2002. Spatial Snow Modeling of Wind-Redistributed Snow Using Terrain-Based Parameters. *Journal of Hydrometeorology*, **3**, 524–538, 10.1175/1525-7541(2002)003<0524:SSMOWR>2.0.CO;2.

SUPPLEMENTARY MATERIAL

Snow-deposition characteristics from SAR and geospatial analysis at Union Glacier, Antarctica

Christian Florian Göbel (cfgobel@gmail.com), Jorge Arigony-Neto, Ricardo Jaña, Rodrigo G omez Fell, Jean de Almeida Espinoza, Francisco Fernandoy, Ian D. Goodwin, Gulab Singh

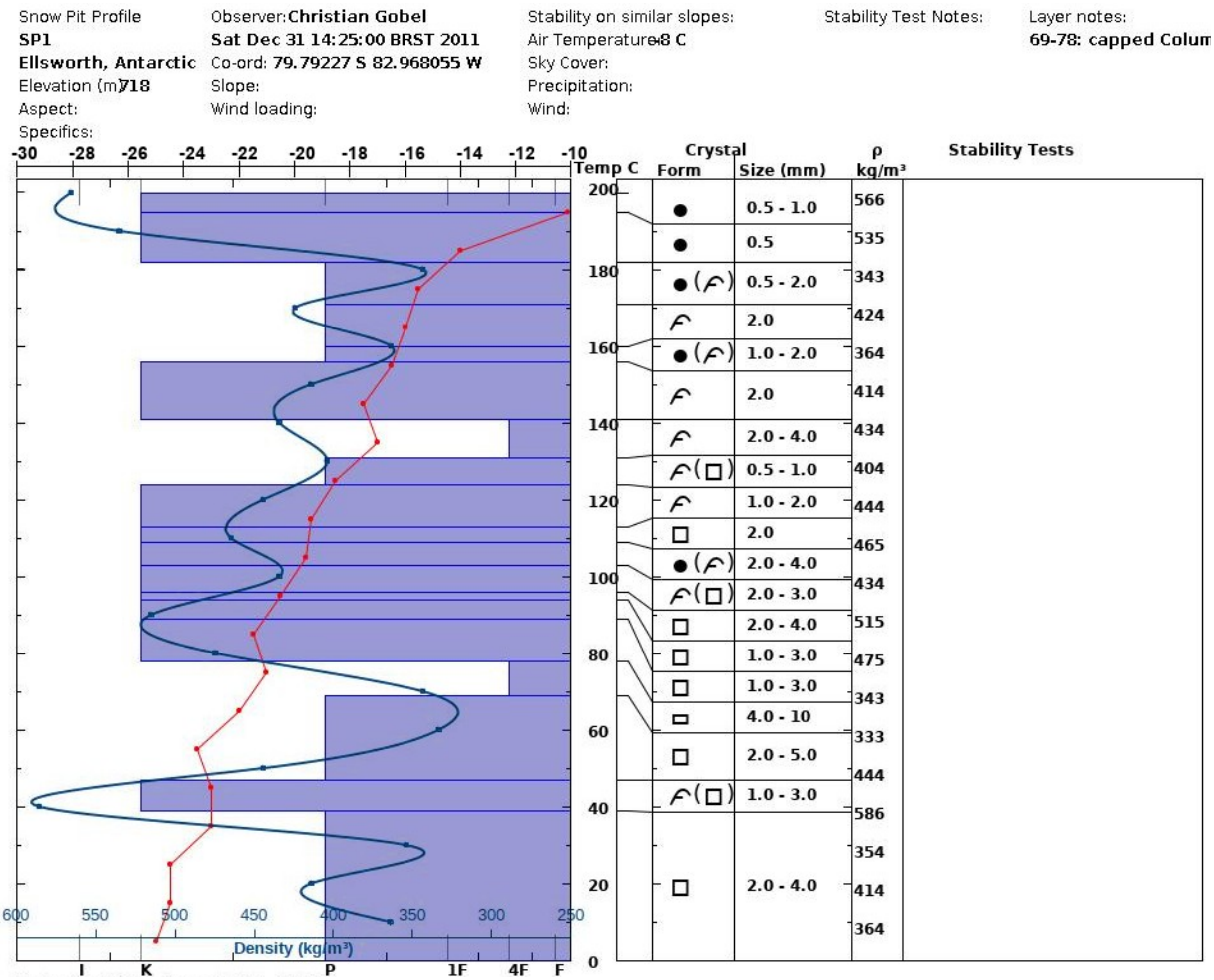

Supplementary Figure S1: Snowpit 1 diagram. Temperature profile plotted in red with the top axis. The bars indicate hand hardness with the bottom axis. Density profile plotted in blue with the axis at bottom above the hand hardness axis.

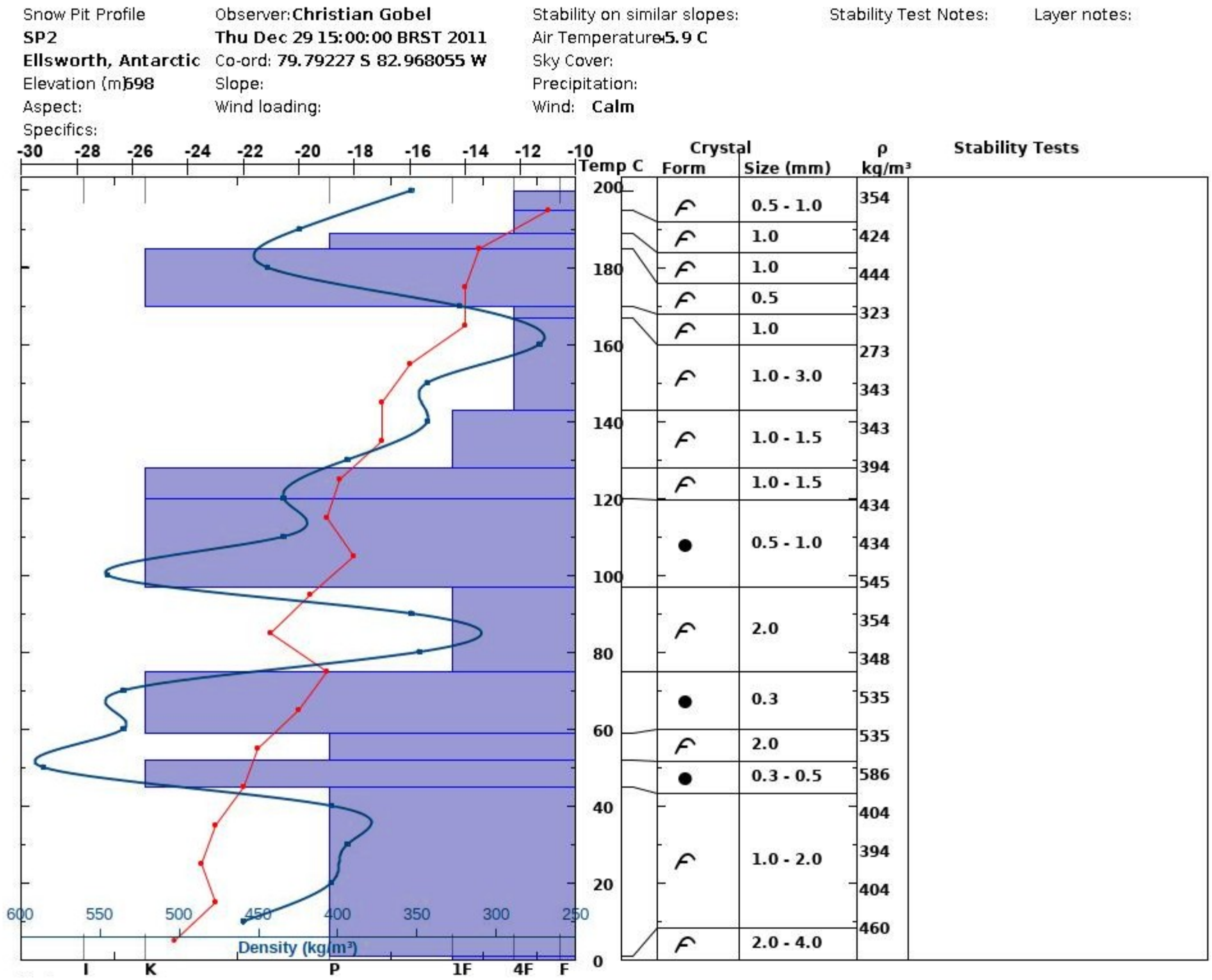

Supplementary Figure S2: Snowpit 2 diagram. Temperature profile plotted in red with the top axis. Th e bars indicate hand hardness with the bottom axis. Density profile plotted in blue with the axis at bott om above the hand hardness axis.

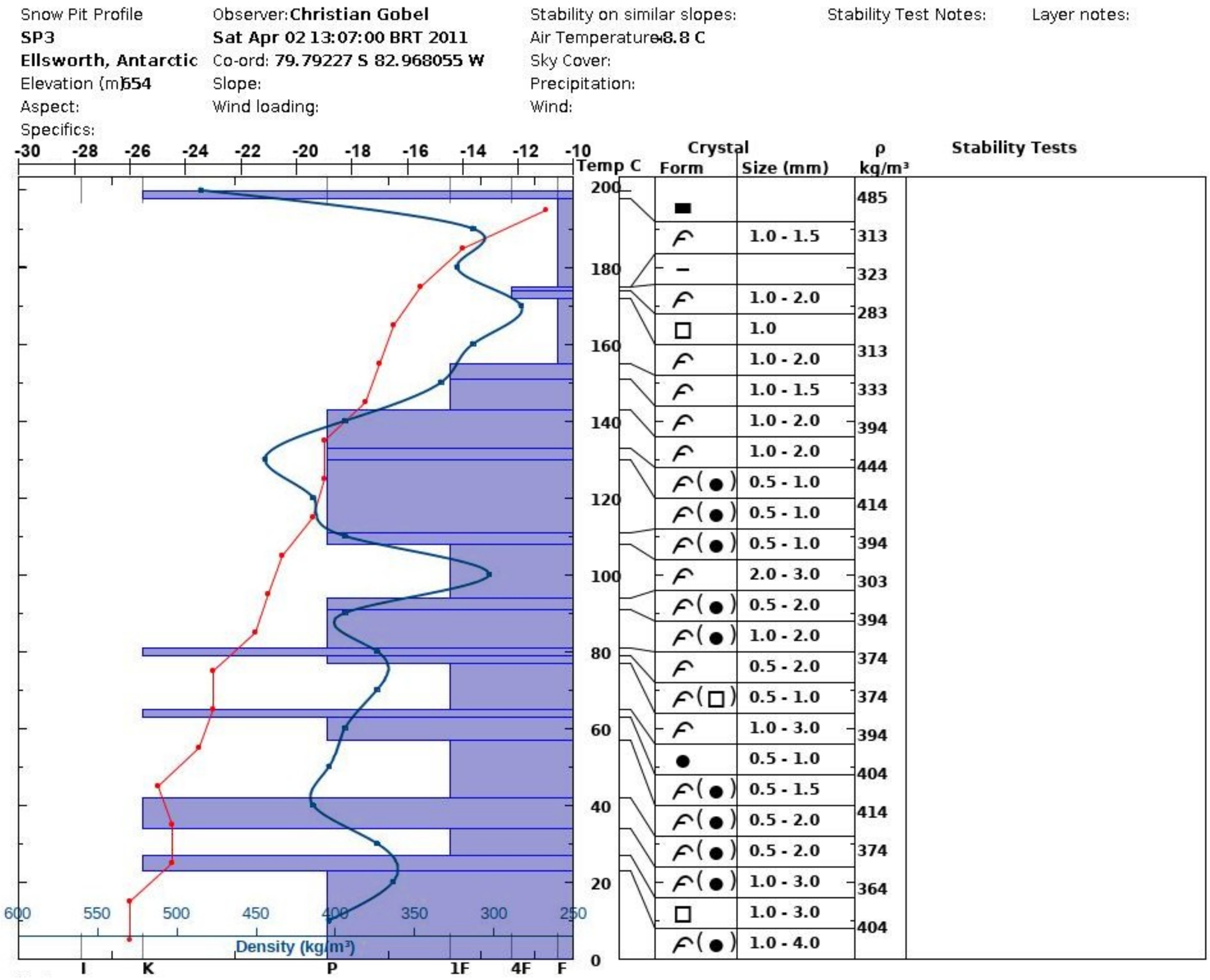

Supplementary Figure S3: Snowpit 3 diagram. Temperature profile plotted in red with the top axis. The bars indicate hand hardness with the bottom axis. Density profile plotted in blue with the axis at bottom above the hand hardness axis.

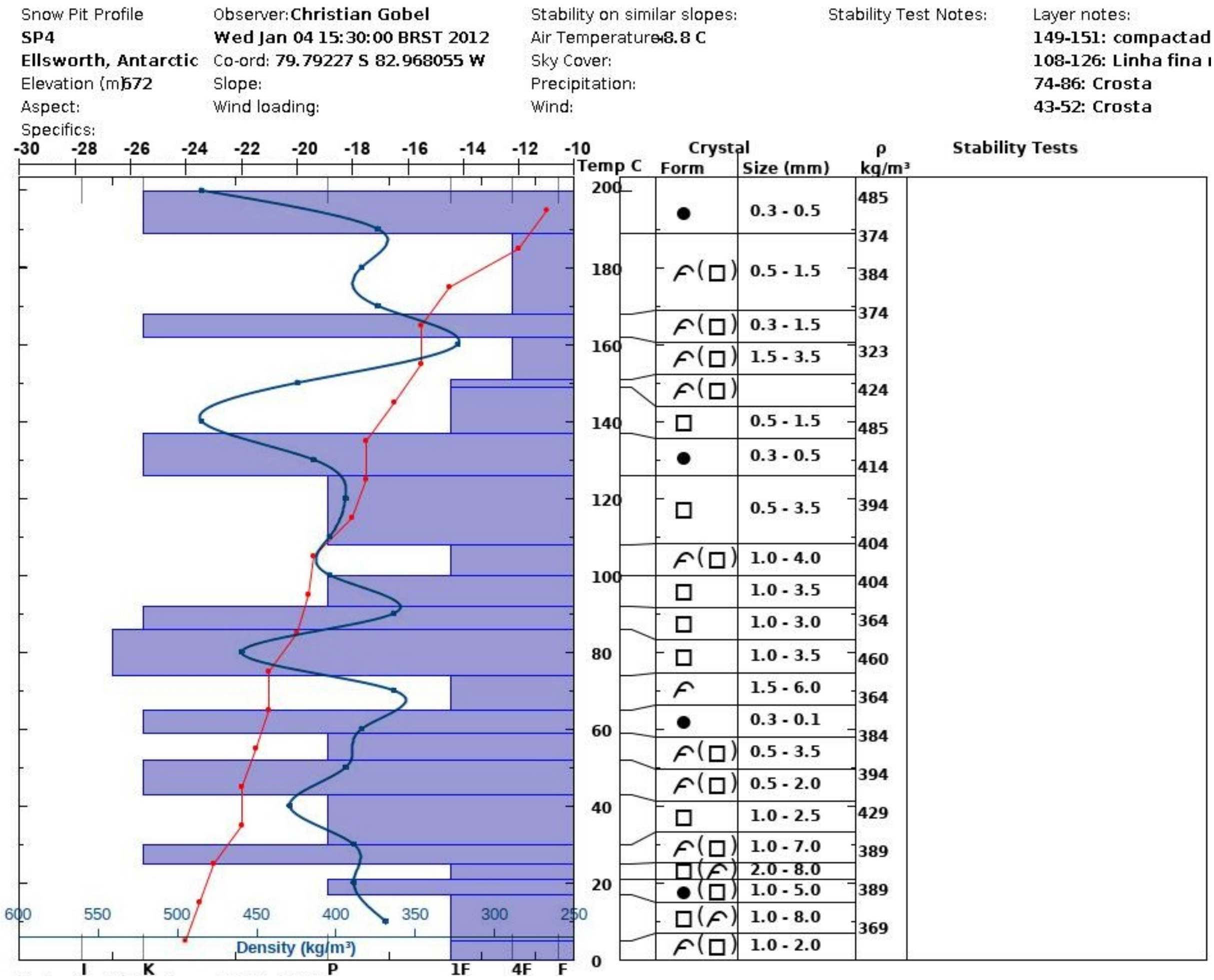

Supplementary Figure S4: Snowpit 4 diagram. Temperature profile plotted in red with the top axis. The bars indicate hand hardness with the bottom axis. Density profile plotted in blue with the axis at bottom above the hand hardness axis.

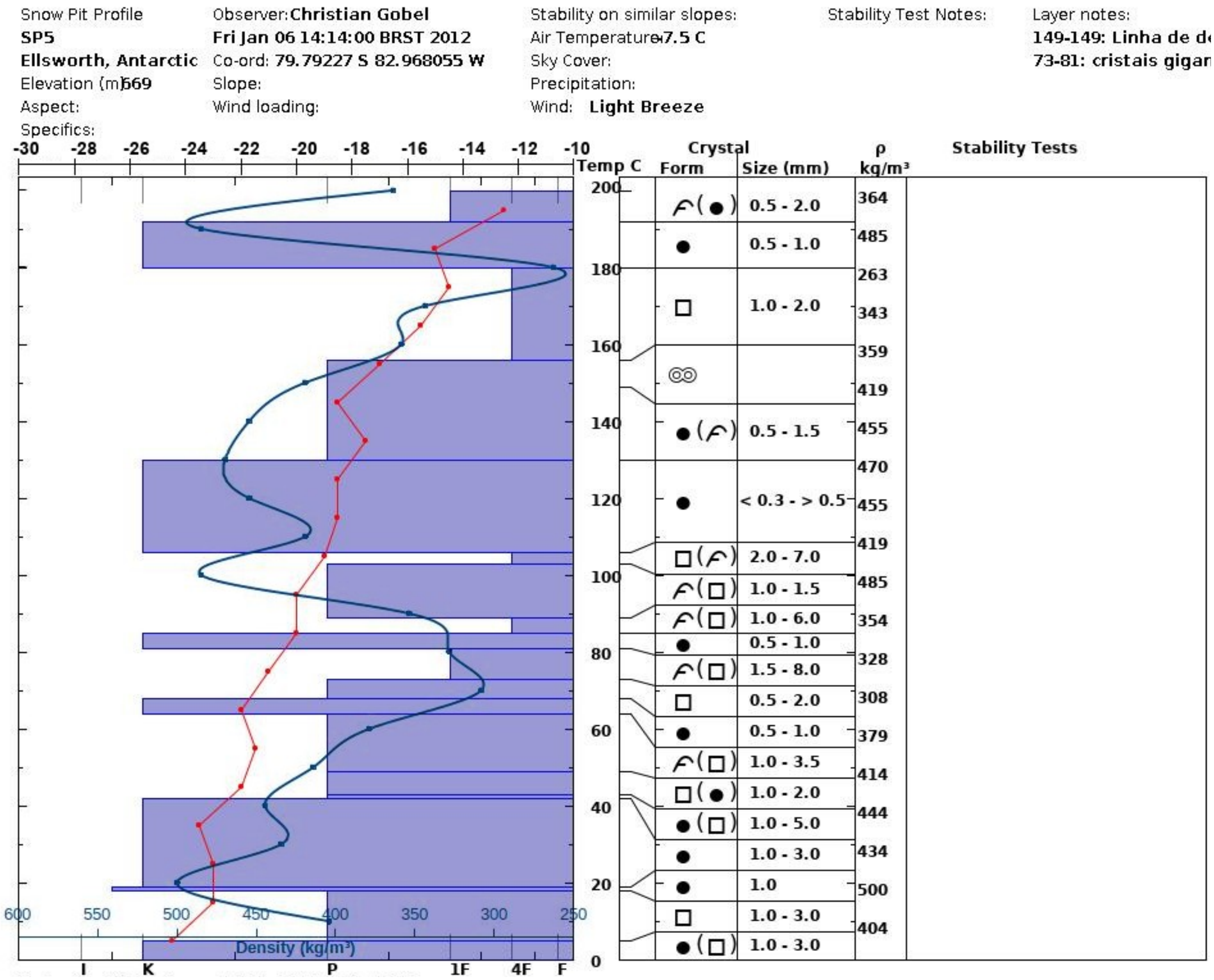

Supplementary Figure S5: Snowpit 5 diagram. Temperature profile plotted in red with the top axis. The bars indicate hand hardness with the bottom axis. Density profile plotted in blue with the axis at bottom above the hand hardness axis.

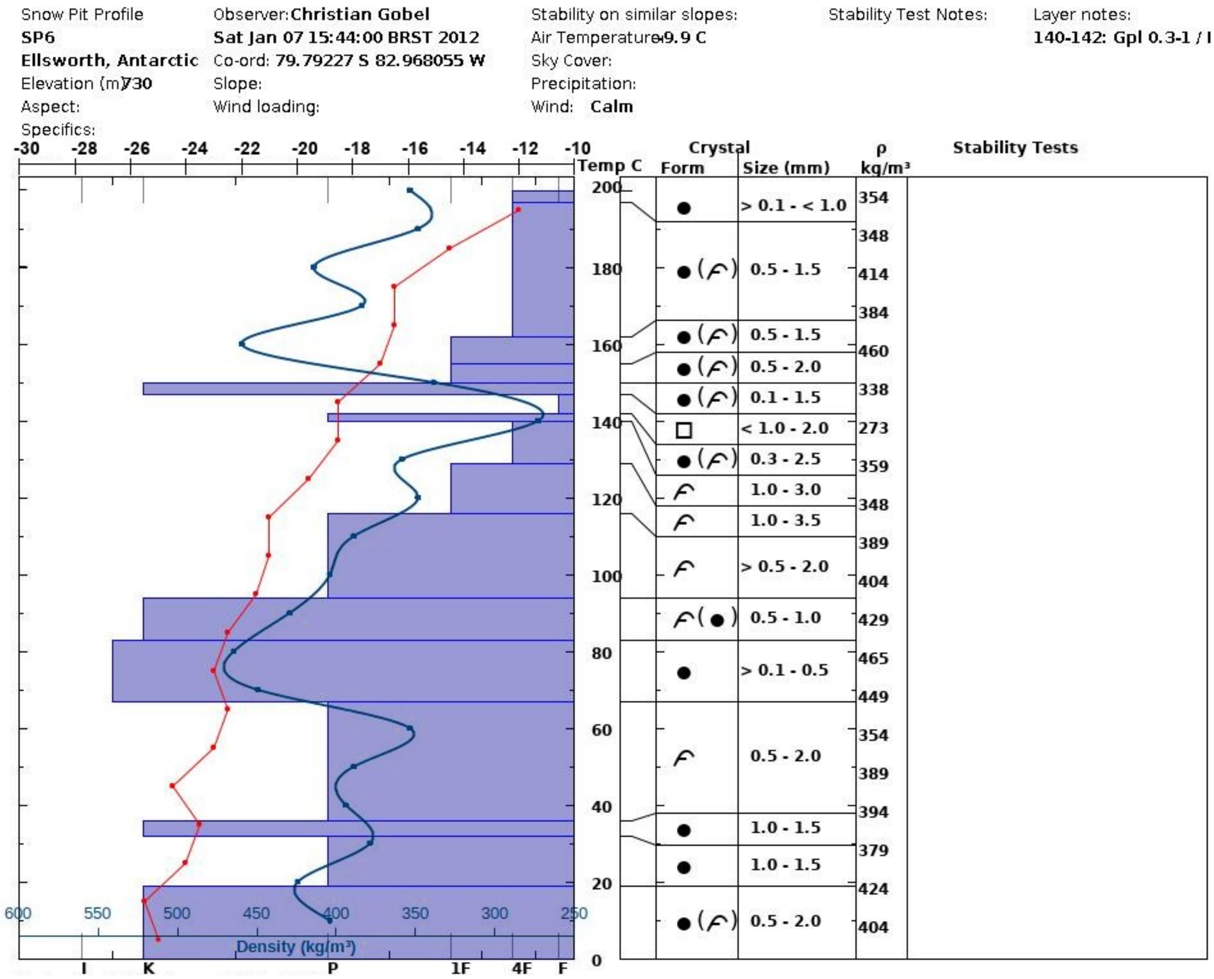

Supplementary Figure S6: Snowpit 6 diagram. Temperature profile plotted in red with the top axis. Th e bars indicate hand hardness with the bottom axis. Density profile plotted in blue with the axis at bott om above the hand hardness axis.

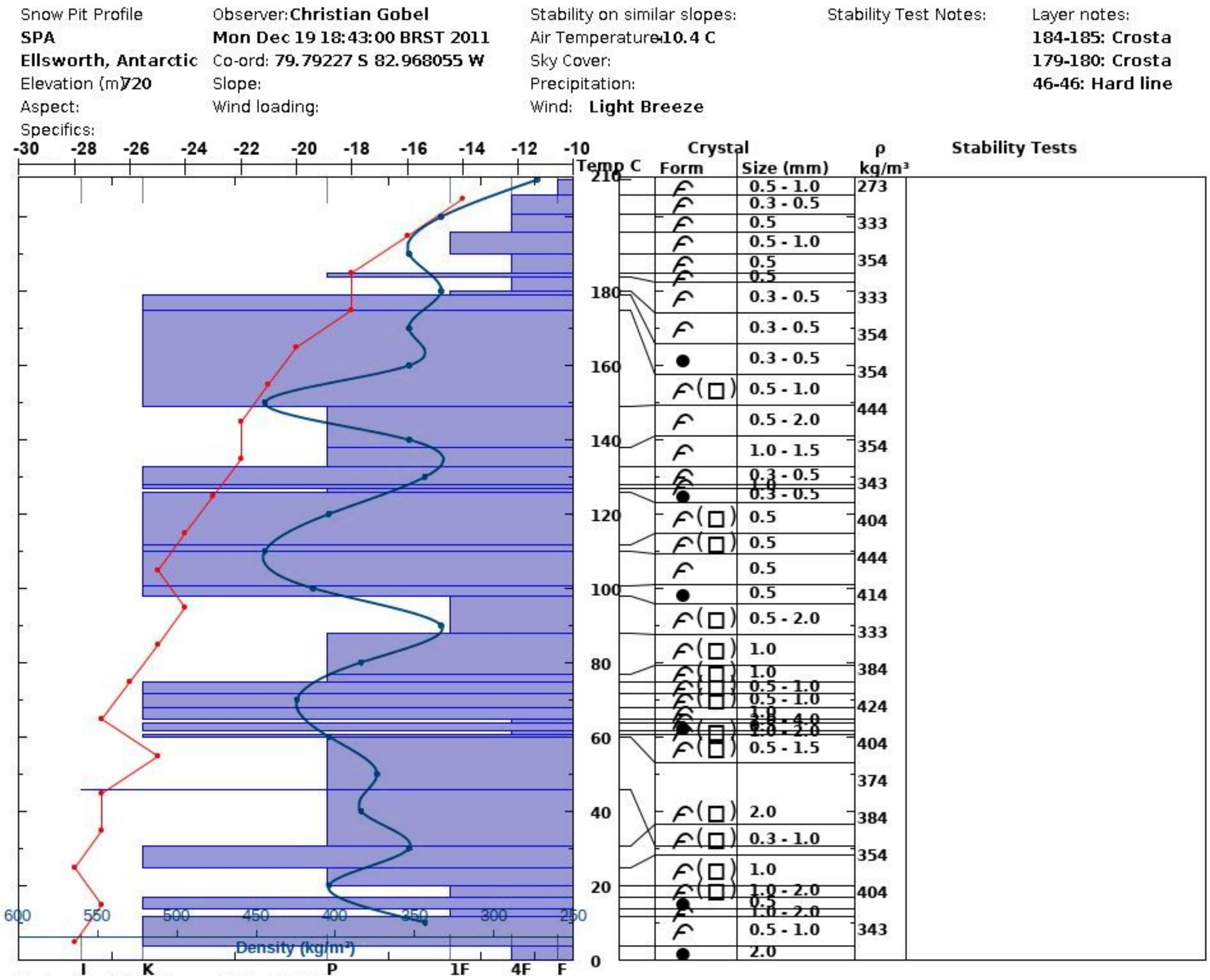

Supplementary Figure S7: Snowpit A diagram. Temperature profile plotted in red with the top axis. The bars indicate hand hardness with the bottom axis. Density profile plotted in blue with the axis at bottom above the hand hardness axis.

Scatter Plot - Hexbins

We plotted each variable against sigma in hexbin scatterplot because of the high densit y of data. No clear cluster of values is observed.

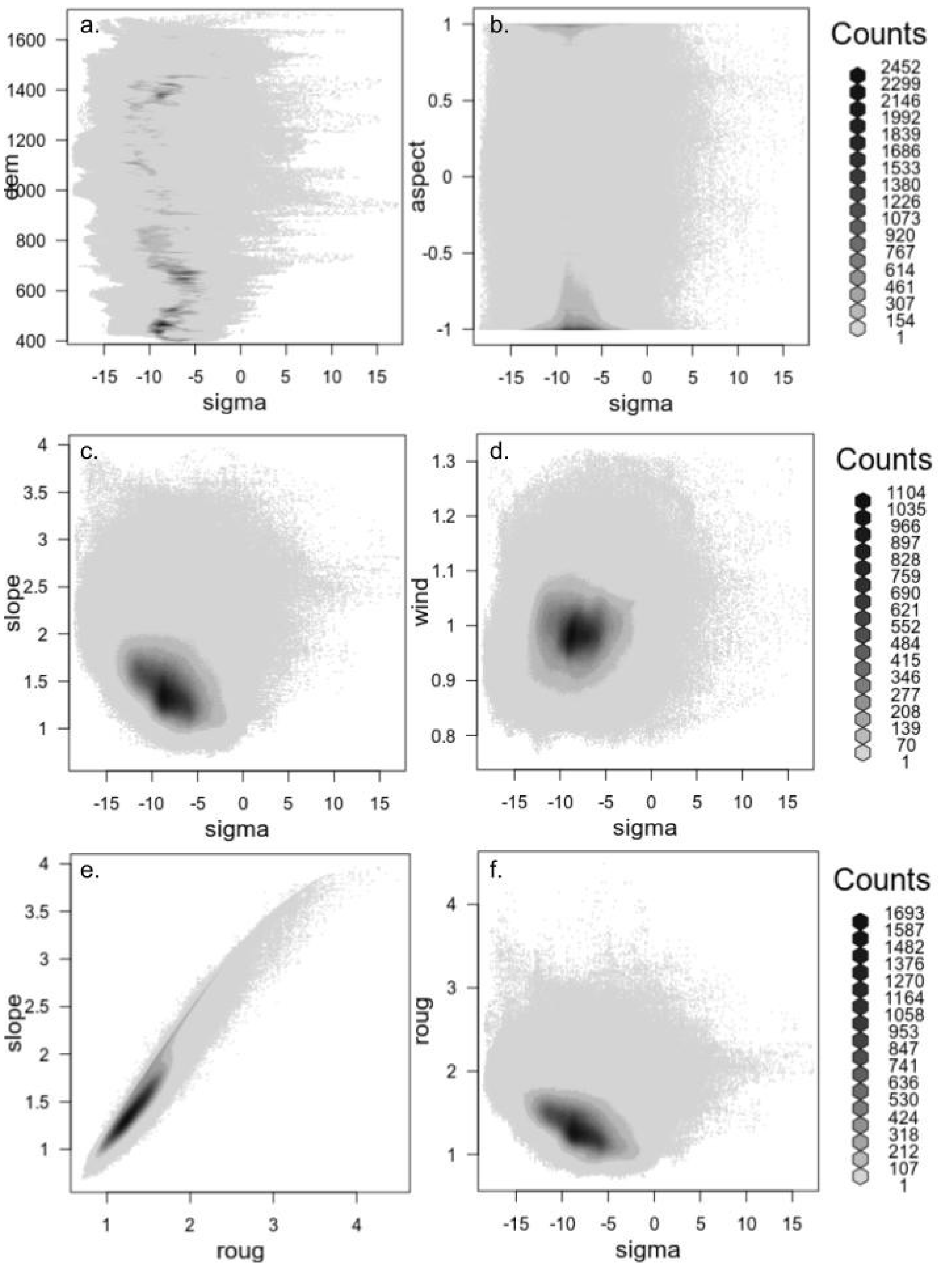

Supplementary Figure S8: Scatterplot in hexbins for each terrain product against sigma values, except for (e.) which is slope against roughness. (a.) elevation values; (b.) relative surface aspect to azimuth o f the prevailing wind direction where, 1 correspond windward and -1 leeward aspect; (c.) slope expres sed in cubic square root; (d.) wind effect where, values <1 indicate wind sheltered and >1 wind expose d areas; and (f.) roughness also expressed in cubic square root.

Elbow test

We did the Elbow test selecting only roughness, slope, dem and sigma. The result do not prese nt a clear elbow:

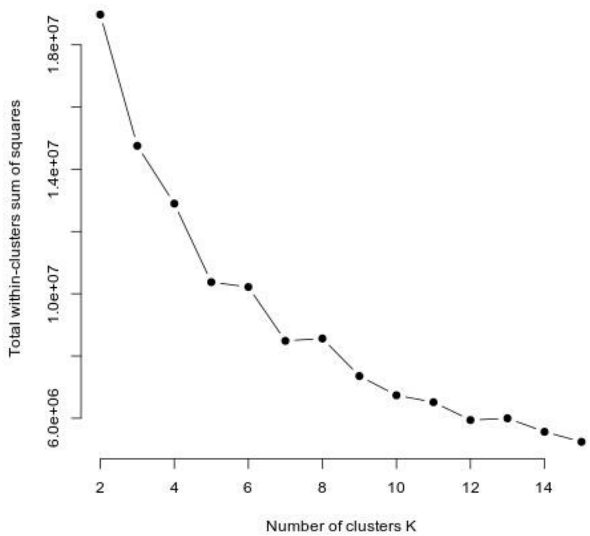

Supplementary Figure S9: Plot of the sum squared error (SSE on the y-axis) for all the pixels in the clu stering analysis with roughness, slope, dem and sigma as input and the number of cluster groups k (x-axis). The elbow method suggests that the number k should be at the point where increasing k provides little return when decreasing the SSE.

Relative humidity

From UNION13's AWS

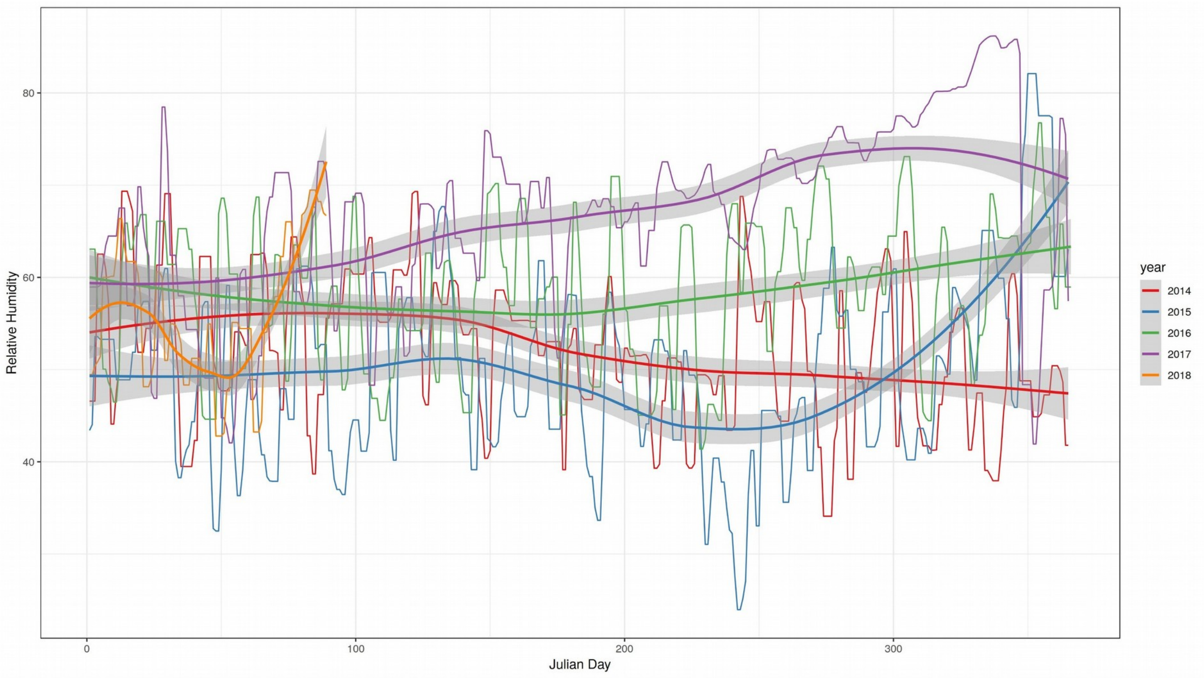

Snow depth from SR50 sensor

Data from UNION13's AWS.

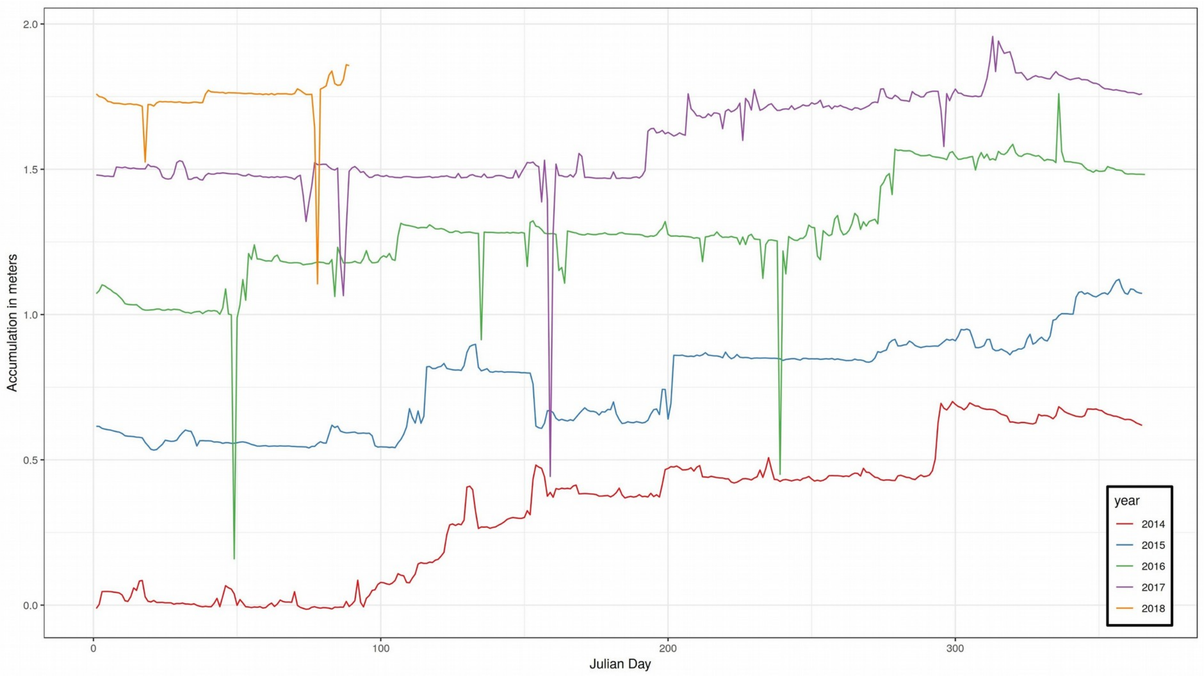

4 Capítulo 4 - Artigo 2

O segundo manuscrito, de autoria de Christian Florian Gobel, Juliana Costi, Ricardo Jaña e Jorge Arigony-Neto, é intitulado **"Influence of snowpack characteristics on TanDEM-X DEM - validation withREMA and field datasets acquired on the Ellsworth Mountains, Antarctica"**, submetido na revista *Geophysical Research Letters*

Neste segundo artigo utilizou-se dois modelos digitais de elevação distintos, comparando-os, para identificar zonas de distintas características do pacote de neve, principalmente no que se refere à taxa de acumulação. Além disso, validou-se os DEMs com dados RTK de campo. A comparação com o segundo modelo baseado em SAR, identificou zonas em que o sinal apresenta uma penetração e interação mais rasa ou profunda com o pacote de neve. Sendo assim, propõe-se o uso dos dois modelos como identificadores da variabilidade espacial na taxa de acumulação da neve.

Influence of snowpack characteristics on TanDEM-X DEM - validation with REMA and field datasets acquired on the Ellsworth Mountains, Antarctica

C. F. Göbel[1,2], J. Costi[3], R. Jaña[4], and J. Arigony-Neto[1,2]

[1]Instituto de Oceanografia, Universidade Federal do Rio Grande, Av. Itália km8, CEP 96201900, Rio Grande, RS, Brazil.

[2]Instituto Nacional de Ciência e Tecnologia da Criosfera (INCT da Criosfera), Rio Grande 96203-900, RS, Brazil.

[3]Instituto de Matemática, Estatística e Física, Universidade Federal do Rio Grande, Av. Itália km8, CEP 96201900, Rio Grande, RS, Brazil.

[4]Departamento Científico, Instituto Antártico Chileno, Plaza Muñoz Gamero 1055, Punta Arenas, Chile.

Corresponding author: Christian F. Göbel (cfgobel@gmail.com)

Key Points:

- REMA validation with field GPS shows that elevation is overestimated by an average of one meter over Union Glacier, Ellsworth Mountains.
- TDX presents higher errors. The deviation is related to snow/ice cover and could be used as a proxy for snow accumulation assessment.
- In Blue Ice Areas, the offset is positive and could indicate a negative SMB. Glacial ice up to 6 m deep influences the SAR backscattering.

Keywords: SAR; GPR; snow accumulation; glacier surface mass balance; blue ice area.

Abstract

The penetration and interaction of X-band synthetic aperture radar (SAR) with snowpack depends on the snow layers physical characteristics related to snow accumulation processes. We use the new Reference Elevation Model of Antarctica (REMA) as a reference surface to subtract from the TanDEM-X elevation model (TDX) and evaluate the X-band interferometric bias in dry snowpack. We confirm the REMA's high accuracy with 70-km-long geodetic measurements on Union Glacier in the Ellsworth Mountains. A mean error of 1.01 ±0.61 meters was found. TDX presented a higher mean error of 2.05 ±2.37 m. We demonstrate that the TDX surface covaries with ice depth and accumulation layering changes in the GPR profiles. Furthermore, we propose that both DEMs' data can be used to investigate the subsurface feature changes and ultimately, the accumulation dynamic changes. Negative (positive) differences indicate high (low or negative) accumulation rate areas where deeper (shallower) penetration occurs.

Plain Language Summary

A key component of understanding the mass balance of Antarctica is surface snow accumulation because of high continental areas and spatial variability. Field measurements are challenging to obtain, and any remote approach aids in understanding this process. We compare the last two high-resolution elevation models available for Antarctica: REMA and TandDEM-X. The first model is derived from visible range satellite images and therefore represents the surface elevation. The latter model is based on radar interferometry at the X-band wavelength, which penetrates and interacts with dry snow. The accumulation rate influences how deep the signal penetrates and consequently offsets the elevation value of the elevation model. We propose a comparison between both data types as a proxy to track areas with distinct accumulation dynamics. Negative (positive) differences indicate high (low or negative) accumulation rate areas where deeper (shallower) penetration occurs.

1 Introduction

A sufficient elevation model for Antarctica is highly necessary to improve the understanding of the physical processes that influence glacier dynamics. On a large scale, surface elevation affects the flow of glaciers and is crucial for atmospheric circulation modeling. The resolutions of continental digital elevation models (DEM) for Antarctica have been improved in the last decades from hundreds of meters, e.g., RADARSAT Antarctic Mapping Project (RAMP) DEM, to tens of meters from stereoscopic medium resolution sensors, e.g., ASTER and ALOS sensor derived global DEM. However, there remains a lack of data and sufficient accuracy for regions inside the continent where homogeneous areas with low feature contrasts occur.

A very high-resolution DEM can represent surface roughness, which influences the deposition and redistribution of snow. The topographic relief can also indicate the depositional characteristics of the surface and subsurface (M. Frezzotti et al., 2002; Goodwin, 1990). Wind plays an important role in the spatial distribution of snow and determines the surface roughness, which is a consequence of the accumulation pattern (Massimo Frezzotti et al., 2004, 2007).

Synthetic aperture radar (SAR) interferometry-derived DEM presents both high resolution and accuracy. A drawback of the method is the signal penetration on the dry snow surface and the need to precisely correct the depth of the interferometric center point. The penetration of the SAR signal in the snow depends mostly on the dielectric constant, in addition the band frequency, which varies according to density, grain size and layering (Forster et al., 1999; Rott et al., 1993; Tsang et al., 2006). These characteristics are directly linked to the accumulation rates in a specific zone (Dierking et al., 2012), and in complex topographic areas such as the Ellsworth Mountains, high spatial variability occurs. Thereafter, a single constant correctness value cannot be expected for a broad area. Wessel et al. (2016) evaluated the TanDEM-X elevation model (TDX) for Greenland with ICESat and found that the SAR penetration was up to 10 m, and the resulting DEM should represent the X-band reflective surface. In other words, the resulting interferometric SAR measurements represent the surface elevation corresponding to the mean phase center of the backscattered signal (Rizzoli, Martone, Gonzalez, et al., 2017). A constant bias is calculated and applied based on the mean height difference between the TDX and ICESat elevations within selected fixed boxes in areas of homogeneous backscattering. Beginning from these fixed blocks, all other Antarctica acquisitions are adjusted by relying solely on tie points and previously calibrated areas.

The recently released REMA DEM is derived from very high spectral resolution images by stereoscopy, and therefore, these data trustworthy representations of the surface-independent surface cover characteristics. We test our first assumption by validating the DEM with field geodesic measurements. We compared both DEMs to identify the zones where the TDX presented penetration depths that are deeper or shallower than the constant bias parameter applied in the TDX product generation. We proposed that the TDX-REMA approach can retrieve the spatial variability of snow accumulation rates, allowing us to delimit and quantify zones with higher accumulation rates, especially where the SAR signal penetrates deeper in the snowpack.

2 Materials and Methods

GPS data. Geodetic measurements were taken during the 2014 summer campaign with the kinematic Global Positioning System (KGPS) method using Leica® equipment. The global positioning system (GPS) points were postprocessed using Precise Point Positioning (PPP) from the base station installed at the EPCCGU base camp. The track points were collected during field displacement on a snowmobile with velocities ranging from 10-20 km h^{-1}. We excluded all points with planimetric, altimetric or absolute accuracies greater than one meter. We snapped the dense point dataset to the nearest neighboring pixel of REMA's common grid. Pixels with varying numbers of points were simplified to a single mean value. The majority of pixels had only two GPS points fused, and 85% had only 3 points.

DEM accuracy assessment. We used the GPS data to validate the REMA accuracy, as we wanted to use it as a reference surface for comparison to TDX. First, we validated both elevation models by calculating the height difference by subtracting the GPS elevation from the corresponding DEM pixel ($\Delta h = h_{DEM} - h_{GPS}$). Here, we understood and assessed accuracy in the same way as Wessel et al. (2018), where the systematic error is estimated by a statistical bias and the random error is estimated by the deviation in the height difference. We excluded height differences greater than 3 deviations before calculating the statistics. Considering a normal distribution, we assess the error by calculating the

mean error (ME), $$ME = \frac{1}{n}\sum_{i=1}^{n} \Delta h_i;$$

root mean square error (RMSE), $$RMSE = \sqrt{\frac{1}{n}\sum_{i=1}^{n} \Delta h_i^2};$$

and standard deviation (STD), $$STD = \sqrt{\frac{1}{n-1}\sum_{i=1}^{n} \left(\Delta h_i - ME\right)^2}.$$

Other measures for accuracy assessment with non-normal error distributions were also calculated as proposed by Höhle and Höhle (2009), where $m_{\Delta h}$ is the median, i.e., 50% quantile:

median absolute deviation (MAD), $$MAD = median_j\left(\left|\Delta h_j - m_{\Delta h}\right|\right);$$

the normalized median (NMAD), $$NAMD = 1.4826 \cdot median_j\left(\left|\Delta h_j - m_{\Delta h}\right|\right);$$

and the absolute deviation at the 90% quantile (LE90) or linear error at the 90th percentile confidence level, $$\mathrm{LE90} = \grave{Q}_{|\Delta h|}(0.9).$$

REMA data. REMA was constructed from stereoscopic imagery collected by four commercial satellites operated by DigitalGlobe Inc., with submeter resolution. The high spatial and radiometric resolutions of these imagers enable high-quality elevation extraction over low-contrast surfaces, such as snow cover and ice sheet interiors/accumulation zones. The REMA mosaic presents 68th and 90th percentile errors of 0.63 and 1.00 meters, respectively (Howat et al., 2019). The acquired strip DEMs that composed the tiles were collected between 2009 and 2017; however, most of the tiles were collected in 2015 and 2016. The tiles are delivered in polar stereographic projection with a posting resolution of 8 meters. We used the REMA grid as a common grid reference for all reprojection and processing steps.

TanDEM-X data. The German Aerospace Center delivers TDX tiles in the geographic coordinates projection, posting in degrees resolution equivalent to an approximately 12x6 m resolution. First, we mosaicked the tiles to cover the Union Glacier (UG) basin and reprojected it to a polar stereographic projection (EPSG:3031) with bilinear resampling to REMA's common grid with an 8 m resolution. TDX images from Antarctica were acquired during the austral winter, between May and July 2013, and during the same months in 2014 (Rizzoli, Martone, Gonzalez, et al., 2017). The global validation performed by these authors confirmed an absolute height accuracy of 3.49 m at the 90% confidence level, which is well below the 10 m mission specification. A second assessment with GPS data with an accuracy of less than 0.5 m confirmed an even lower error of below 2 m (Wessel et al., 2018). Because these accuracy assessments did not include Antarctica, we assessed the height error annotated within the height error map (HEM) of the TDX product, as the HEM is a good estimate of the theoretical random height error (Wessel et al., 2018).

DEM differences. The time interval between both DEMs is between 2 and 4 years. Rivera et al. (2014) reported a mean local elevation change at the narrow flux gate of -0.012 m a^{-1}, an amount close to the estimated error of the measurements, which also indicates near-equilibrium conditions. We also confirmed no elevation changes between 2005 and 2009 from the ICESat-GLAS passes, with differences of less than one meter. For this reason, we performed a comparison between both DEMs considering no surface elevation change. We subtracted REMA from TDX. Because of the penetration of the SAR signal in the snow and the influence of surface roughness, high-frequency noise is inherited in the TDX product. Each REMA strip DEM that is composited with the mosaic product is filtered and downsampled to a 32 m grid during the CryoSat-2 registration process (Howat et al., 2019). Therefore, we filtered the TDX using a moving average filter with a window of 5x5 pixels (40x40 m), and we refer to this as TDX_A5. The result is a smoother surface similar to that of REMA, and the different height map presented in the results section is more homogeneous, representing a regional tendency that is higher or lower than REMA.

Masked areas. As we aimed to assess higher accumulation rate zones, where the SAR signal presented higher penetration, we masked the well-delimited bare ice surfaces with the blue ice area (BIA) mask (Hui et al., 2014). We also mask areas with moderate to high slopes that are greater than 5º (~10%). The mask polygons are depicted in Figure 1. The slope mask separated the mountainous and rocky areas and simultaneously reduced the geometry's influence on the SAR signal. BIAs in slope areas that were greater than 5º were considered to be steep areas.

GPR data. GPR profiles were collected using GSSI SIR® System-3000 with a 400 MHz antenna in the 150 ns range (~12 m depth in dry snow) for the same 70 km displacement over UG (Figure 1). We also collected data in the 600 ns range in the central valley to track the firn depth up to 60 m. All data were collected in time mode and were not automatically synchronized with GPS. The GPS acquisition was postprocessed in GIS software to precisely georeference and topographically correct each GPR profile. We analyzed profiles where the firn/ice interface was detectable and extracted the depth values of these transects.

3 Results

To validate and assess the REMA and TDX height accuracies, we compared the elevation data with the GPS dataset. We used approximately 13 k grid points, and of these grid points, ~10.5 k were on a flat snow surface, ~1.5 k were in BIAs exclusively, and ~1 k were in steep areas. The statistics of the height differences are summarized in Table 1. In the supporting information (SI), we presented the surface elevation profiles of the 3 datasets. The GPS ME indicates an overall REMA offset of 1.01 with consistency through all classes. The profiles show a smoother surface due to the rough terrain filter in the strip DEM registration (Howat et al., 2019), and an excellent representation was confirmed, which reflected the low standard deviation. The REMA has an STD (0.60 m) that was nearly half the RMSE (1.17 m). The STD is slightly greater than the NAMD (0.45 m), indicating a good approximation to a normal distribution. The NMAD is a more robust measure for the 68% probability level than the RMSE or standard deviation. At the 90% probability level, the linear error LE90 is 1.73 m, which is greater than the 1.00 m reported by (Howat et al., 2019), but this result is expected for rougher terrain. Therefore, we assumed that REMA is a good reference surface for further comparison to TDX.

The TDX presents a higher RMSE for all GPS points (3.27 m) and a great deviation in the height differences (2.54 m). The NMAD and LE90 were 2.63 and 5.64 m, respectively. These values are greater than the global absolute height accuracy of 3.49 m (Rizzoli, Martone, Gonzalez, et al., 2017), which is clearly influenced by BIA and shallow snow/ice layer. There is a divergence between each considered class due to a change in backscattering in each class. The ME error of 5.04 m and low NMAD in BIAs indicates a consistent offset of the elevation over these areas, where the calculated height values are offset by the constant correctness in the registration step of the mosaic. The TDX profiles presented high-frequency variances in elevation. These variances are observed in some of the GPS profiles with smaller amplitudes, e.g., 'Long-Driscoll' profile (Figure S25). This high frequency represents the surface roughness, but in TDX, the high frequency is enhanced by subsurface layering structures. The filtered DEM (TDX_A5) presented a small decrease in all statistical parameters but maintained a close standard deviation compared to the nonfiltered DEM.

The TDX profiles have a consistent positive difference over the BIAs. The same is observed in a surrounding buffer zone, which is probably due to the shallowness of the glacial ice. This bias is approximately 5 m and reflects the positive offset correction applied to the mean phase center of the backscattered signal. Otherwise, the TDX shows agreement with the GPS profile rather than with REMA, with the exception being in zones where the TDX gets deeper than the GPS values, which we proposed to be related to the high accumulation zones.

Table 1. (**GPS POINTS Table**) Height accuracy assessments of each DEM against the field GPS. TDX_A5 is the average 5x5 filtered DEM. (**TDX-REMA Table**) Model-based accuracy analysis of TDX with REMA. Notably, we considered the TDX_A5 to be equivalent to a smoother REMA. A statistical summary was calculated in the classes of flat snow, BIA and steep areas as described in the text.

GPS POINTS							
Class	Points	ME (m)	RMSE (m)	STD (m)	MAD (m)	NMAD (m)	LE90 (m)
flat snow	10535	0.99	1.12	0.53	0.30	0.45	1.66
BIA	1511	1.05	1.18	0.55	0.23	0.35	1.59
steep	886	1.03	1.53	1.12	0.58	0.86	2.50
REMA - ALL	**13326**	**1.01**	**1.17**	**0.60**	**0.31**	**0.45**	**1.73**
flat snow	10560	1.55	2.75	2.27	1.46	2.16	4.97
BIA	1509	5.18	5.34	1.29	0.67	0.99	6.63
steep	1025	2.52	4.24	3.41	1.98	2.93	7.55
TDX - ALL	**13503**	**2.05**	**3.27**	**2.54**	**1.78**	**2.63**	**5.64**
flat snow	10562	1.29	2.51	2.15	1.04	1.55	4.81
BIA	1511	5.20	5.33	1.16	0.49	0.73	6.49
steep	998	2.61	4.27	3.38	1.17	1.74	8.11
TDX_A5 - ALL	**13480**	**1.82**	**3.09**	**2.49**	**1.33**	**1.98**	**5.49**

TDX_A5 - REMA							
Class	Points	ME (m)	RMSE (m)	STD (m)	MAD (m)	NMAD (m)	LE90 (m)
flat snow	107360150	-0.07	1.29	1.29	0.79	1.17	1.53
BIA	4084824	4.64	4.92	1.66	0.98	1.45	6.40
steep	12815811	2.93	5.12	4.20	2.86	4.24	8.57
ALL UG pixels	**123434747**	**0.37**	**2.12**	**2.09**	**0.92**	**1.37**	**2.83**

The DEM validation showed that REMA can be used as a reference surface. It is possible to compare TDX and REMA and assume that the spatial difference between both is a function of the X-band attenuation depth of the TDX data. This model-based accuracy assessment is summarized in (TDX_A5-REMA) Table 1, and the histogram of the height differences is presented in the SI (Figure S6). All results were calculated with the original TDX, not the filtered TDX. For all pixels, the histograms approximate a normal distribution, which is narrower but tailed to positive values for the contributions of mountain areas and BIAs. The mean height difference of 0.37 m indicates that TDX is close to REMA, and considering only flat snow cover areas, the mean difference is only -0.07 m.